ORIGINAL PAPER

The use of a multiscale approach in electrochemistry to study the corrosion behaviour of as-cast AZ91 magnesium alloy

Iwona Kot[1] · Halina Krawiec[1]

Abstract The microstructure of as-cast AZ91 alloy is complex, with the presence of $Mg_{17}(Al, Zn)_{12}$ precipitates surrounded by an eutectic phase, AlMn intermetallic particles and an α-Mg solid solution. In addition, the distribution of aluminium in the alloy was found to be heterogeneous. Under these conditions, a multiscale approach coupling global and local electrochemical measurements seems to be a promising method to study its corrosion behaviour. Results show that the multiscale approach can be used in 0.1 M NaCl. In this case, AZ91 is susceptible to pitting corrosion. By contrast, the multiscale approach is not valid for AZ91 in 0.1 M Na_2SO_4. At the global scale, filiform corrosion and pitting corrosion are observed in the matrix, whereas only pits initiate when using the microcapillary techniques. The obtained results show that the local electrochemical techniques have to be used carefully in some environments.

Introduction

Magnesium alloys are commonly used as structural materials in the automotive and aerospace sectors by virtue of their low densities and high strength-to-weight ratios. However, in spite of such attractive mechanical properties, their relatively low corrosion resistance is a serious obstacle to their widespread application [1–4]. On account of its relatively low cost and excellent castability, AZ91 is one of the most widely used magnesium alloys [5]. It has been shown that its chemical composition has a fundamental influence on its corrosion behaviour and mechanical properties [5–9]. The addition of rare earth elements improves the mechanical properties of magnesium alloys, especially the ultimate tensile strength, but decreases their corrosion resistance [6, 9]. Furthermore, the presence of a small amount of bismuth and antimony significantly increases the corrosion rate of magnesium alloys [10]. By contrast, some alloying elements such as silicon and calcium enhance the corrosion resistance of magnesium alloys [7, 9]: calcium improves the corrosion resistance through the formation of the reticular Al_2Ca phase, which acts as an effective barrier against corrosion, while the combined addition of Si and Sb enhances the corrosion resistance of AZ91 alloy [7]. It has been shown that the addition of calcium oxide to AZ91 alloy improved its corrosion resistance due to higher pitting potential and the refinement of the precipitates [11]. A number of additions also ennobled the corrosion potential of AZ91. Addition of some elements, such as Cr, Mo and Y, leads to a shift of up to approximately 20 to 50 mV towards more positive potential values. It was also noted [8] that the addition of Y (1 or 2 wt%) induces a shift of the AZ91 corrosion potential to the anodic direction. By contrast, addition of a low content of Y (0.1 at.% Y) induces a significant decrease of the corrosion potential.

Many studies [12–32] have revealed that the corrosion behaviour of AZ91 alloy depends on the aluminium content and microstructure, particularly the amount and distribution of intermetallic phases and inclusions. The influence of intermetallic phases on the corrosion behaviour of magnesium alloys has been investigated in a number of papers [4, 13, 14, 16–21, 23–30, 32, 33]. It has been shown that an increase in Al content (8–9 wt%) significantly improves the corrosion resistance

✉ Halina Krawiec
krawiec@agh.edu.pl

1 Faculty of Foundry Engineering, AGH-University of Science and Technology, Reymonta 23 Street, 30-059 Cracow, Poland

of these alloys [23]. The AZ91 alloy consists of two interme-tallic phases: β-$Mg_{17}Al_{12}$ and η-Al_8Mn_5. The presence of a eutectic structure has been observed around the β-phase. Song et al. [26, 29] showed that in sodium chloride solution, the free corrosion potential of the β-phase was 0.3 V more positive than that of the α-phase, and this difference in free corrosion potential was observed to cause microgalvanic corrosion. Ac-cording to results obtained through Scanning Kelvin Probe Force Microscopy, the β-$Mg_{17}Al_{12}$ and η-Al_8Mn_5 phases act as local cathodes when coupled to the α-magnesium phase (matrix) under atmospheric conditions [17]. Moreover, strong dissolution of the matrix has also been detected around these particles [19, 20]. Other studies [34, 35] have confirmed that the α-phase is less noble than β-$Mg_{17}Al_{12}$. The higher corro-sion resistance of the β-phase has been attributed to the for-mation of a passive film on its surface [15, 18]. A similar occurrence was observed for η-Al_8Mn_5 particles in 1 M NaOH; this was followed by the formation of pits around these particles [36]. It has been shown that β-$Mg_{17}Al_{12}$ plays a dual role in the corrosion resistance of AZ91 alloy [24–26, 32]. Indeed, it can act as either a barrier or a galvanic cathode: as mentioned above, the corrosion potential of β-$Mg_{17}Al_{12}$ has been found to be more positive than that of the α-magnesium phase (matrix), which may therefore accelerate the galvanic corrosion of α-magnesium [21]. On the other hand, β-$Mg_{17}Al_{12}$ can, if present in the form of a continuous network, act as a corrosion barrier and hinder corrosion prop-agation in the matrix [24–26]. Lunder [19] showed that β-$Mg_{17}Al_{12}$ could reduce the corrosion rate of AZ91 by forming a corrosion-resistant barrier through the precipitation of an Al-rich coring structure along grain boundaries.

It has been shown that the eutectic ($\alpha+\beta$) and α-Mg (matrix) phases have different aluminium contents [23, 26]. These dissimilar aluminium distributions give rise to different corrosion behaviours: areas with aluminium concentrations of less than approximately 8 % have been found to be more prone to corrosion attack than areas with higher amounts of aluminium or areas containing the β-phase [13]. Both α-magnesium and the eutectic phase can cause galvanic corro-sion with the β-$Mg_{17}Al_{12}$ phase. According to microelectrochemical measurements performed in 0.1 M $NaClO_4$ solution, the eutectic phase is more susceptible to corrosion than α-Mg (matrix) [37].

The casting method has a primary influence on the micro-structure—and hence the corrosion resistance—of magne-sium alloys. Die-cast material with smaller grain sizes and a fine β-phase has been found to exhibit marginally lower cor-rosion rates and better passivation compared with ingots [13]. Moreover, the heat treatment has influence on the microstruc-ture of AZ91 alloy and its corrosion resistance. It has been shown [38] that the corrosion resistance of AZ91 decreases in 0.1 M NaCl solution as the T6 aging time increases (between 10 and 19 h).

In the present, a multiscale approach coupling global and local electrochemical measurements is applied to AZ91 in 0.1 M NaCl and 0.1 M Na_2SO_4 solutions. Indeed, sulphate ions, like chloride ions, often tend to cause passivity break-down and initiate pitting corrosion. In the literature, small attention has been paid to the behaviour of AZ91 in Na_2SO_4-based solutions. The domain of validity of the multiscale approach is first discussed. The electrochemical response of the system is then discussed taking into account the specimen microstructure and the approach considered (multiscale or global approaches).

Experimental

Materials, specimens and surface preparation

All experiments were performed on AZ91 magnesium alloy (chemical composition (wt%): Zn 0.6, Al 9.03, Mn 0.2, Fe 0.003, Mg 90.2). This alloy was cast at 700 °C in a SF_6/CO_2 gas atmosphere to produce four 100×100 mm^2 plates of dif-ferent thicknesses, namely 10, 15, 20 and 30 mm for plates #1, #2, #3 and #4, respectively. The mould used for the casting was made of a resin that was sand-hardened by CO_2. No heat treatment or plastic deformation was carried out after casting. Microstructural and electrochemical investigations were per-formed on $2\times23\times27$ mm^3 (thickness$\times$width$\times$length) plate specimens, which were mechanically ground with silicon car-bide (SiC) papers down to 4000 grit and polished using dia-mond pastes (3 and 1 μm). All specimens were ultrasonically cleaned in ethanol between each grinding/polishing operation.

Electrochemical measurements and surface observations

The electrochemical behaviour of specimens was studied in 0.1 M NaCl and 0.1 M Na_2SO_4 solutions at room temperature at both the global and local scales. All potentials were mea-sured vs. Ag/AgCl (3 M KCl solution). An AUTOLAB302N electrochemical interface with the Extreme Low Current De-tection (ECD) module was used in order to achieve a current detection of approximately 1 fA. At both scales, potentiody-namic polarisation curves were plotted from −2000 mV vs. Ag/AgCl in the anodic direction at a scan rate of 1 mV s^{-1}.

Local measurements were performed using the electro-chemical microcell technique [39–44]. The set-up for this technique consists of an electrolyte-filled glass capillary whose tip is adhered to the specimen surface with a layer of silicon rubber. The electrolyte used is aerated. This microcell is mounted onto a microscope to enable precise positioning of the capillary on the specimen surface. In our investigations, the capillary tip has a diameter ranging between 30 and 70 μm, depending on the microstructure that is studied. The counter electrode is a platinum wire. Each electrochemical

measurement was repeated six times. As it will be discussed in the next sections, they were reproducible. By contrast, global measurements were carried out using a classical three-electrode cell, whose counter electrode is a 2.5-cm-diameter platinum disc. Global experiments were repeated twice. Results are found to be very reproducible.

A field-emission type scanning electron microscope (JEOL 6400F) with an integrated energy-dispersive spectrometer (FE-SEM/EDS) was used to determine the morphology and chemical composition of precipitates and metallic phases.

Results and discussion

The microstructure of AZ91 was already studied, and results are presented in [37]. In summary, AZ91 has a very complex microstructure composed of α-Mg solid solution (dendrites), β-$Mg_{17}(Al, Zn)_{12}$ precipitates, AlMn intermetallic particles and a eutectic phase (Fig. 1). The chemical composition of these phases and particles is given in Table 1. Moreover, heterogenous distribution of aluminium is observed. Boundaries of α-Mg dendrites are enriched in aluminium (Fig. 1 and Table 1). This necessarily implies highly heterogeneous electrochemical behaviour, which prompts us to study the corrosion behaviour of samples at the microscale using local electrochemical technique. However, it was already shown that under certain conditions, the microcell geometry may affect significantly local electrochemical measurements [42]. Therefore, both local and global (using a classical three-electrode cell) measurements have to be performed. Results obtained at both scales are systematically compared to each other. This is the multiscale approach. From this approach, it will be possible to study the relationships between the microstructure and the corrosion behaviour of AZ91 and to propose metallurgical
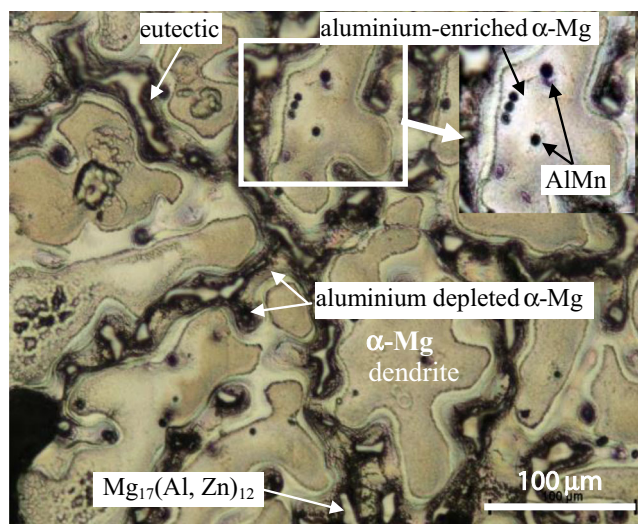

Fig. 1 Optical micrographs of the as-cast AZ91 alloy after etching in Nital solution for 10 s

criteria leading to corrosion. Note that the double-channel microcapillary may be used to make a solution flow and to overcome certain limitations of the microcapillary cell [42, 44]. However, to obtain stable and reproducible results, the diameter of the double-channel capillary must be large (greater than 100 μm). This capillary size is not useful in the present study.

Global and local electrochemical behaviour of AZ91 in 0.1 M NaCl

Figure 2a shows the open circuit potential (OCP) as a function of time for the AZ91 alloy in 0.1 M NaCl at both scales. Figure 2b shows the types of sites that were investigated at the microscale, namely the α-Mg matrix (centre of dendrites), the matrix containing the β-phase, the matrix containing AlMn precipitates and the matrix containing both the β-phase and AlMn precipitates. In this figure, the diameter of the circles corresponds to that of the capillary.

At the global scale (grey curve in Fig. 2a), a steady state is reached after roughly 700 s of immersion. At the local scale, the time necessary to reach a steady state was found to depend on the investigated site. A steady state is also quickly reached in the presence of the matrix with β-phase (red curve in Fig. 2a) or with AlMn particles (blue curve in Fig. 2a). In sites containing β-phase+AlMn+α-Mg matrix (green curve in Fig. 2a), the steady state is only reached after 6000 s of immersion. The OCP values measured at the local scale are between −1345 mV vs. Ag/AgCl (sites with the matrix+β-phase+AlMn particles) and −1640 mV vs. Ag/AgCl (matrix). This confirms that the sample has a heterogeneous electrochemical behaviour. The lowest OCP is recorded for the α-Mg matrix (black curve in Fig. 2a), suggesting that the primary α-Mg phase is the most prone to corrosion. In addition, the OCP measured at the global scale follows the same evolution as that of sites containing the matrix with AlMn (OCP around −1510 mV vs. Ag/AgCl).

Figure 3 shows the polarisation curves of AZ91 in 0.1 M NaCl at both scales. First, it can be observed that in the cathodic domain, the global polarisation curve follows the same evolution as those of sites containing the matrix with AlMn (as it was found for the OCP). Therefore, cathodic reactions occur preferentially in those sites. The anodic branch of the global polarisation curve indicates active behaviour, with a sharp increase in current density as soon as the corrosion potential is reached (of about −1380 mV vs. Ag/AgCl). At these applied potentials, the α-Mg matrix located in the centre of dendrites becomes active (black curves in Fig. 3a). Pitting potentials are between −1350 and −1250 mV vs. Ag/AgCl. The local curves obtained in these sites are very reproducible. Figure 4(a1) and (b1) shows a pit that initiated in one of these types of sites during local potentiodynamic measurements.

Table 1 Chemical composition (in at.%) of phases and particles in the AZ91 alloy determined by means of FE-SEM/EDS. Each value is an average of 10 measurements. The error is the standard deviation

	Al	Mn	Mg	Zn	O	Ni	Cu
AlMn	38.1±2.0	44±5.0					
β-Mg$_{17}$(Al, Zn)$_{12}$	33.3±3.0	0.3±0.05	61.3±4.0	3.4±0.8	1±0.06	0.37±0.02	0.2±0.05
Centre of dendrites	2.9±0.7		96.9±3.0				
Boundaries of dendrites	7.1±1.0		90.6±2.0	0.5±0.03			

The polarisation curves of sites containing both the matrix and the β-phase are also reproducible (red curves in Fig. 3b). The values of the pitting potential measured at these sites are similar to those for the matrix in the centre of dendrites, ranging between −1350 and −1250 mV vs. Ag/AgCl. Thus, it appears that pits initiate in the matrix, and the presence of the β-phase at these sites has virtually no influence on the

value of the pitting potential. No significant differences are also observed in the current density in the cathodic domain and in the corrosion potentials between black (matrix) and red (β-phase+matrix) curves in Fig. 3a, b. Subsequent surface observations confirm this hypothesis. We observe that many pits initiate at regions in the matrix far from the β-phase (cf. Fig. 4(a2) and (b2) and site 1 in Fig. 4(b3)). Nonetheless, there are some other pits that initiate at the interface between the matrix and the β-phase (sites 2 and 3 in Fig. 4(b3)). It is interesting to note that the role of β-phase may be affected
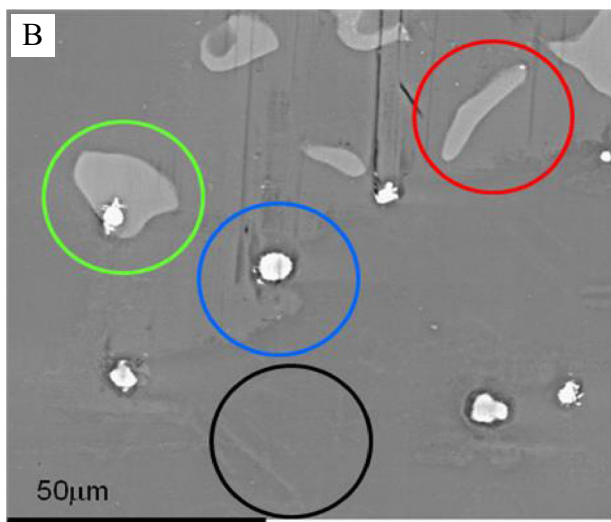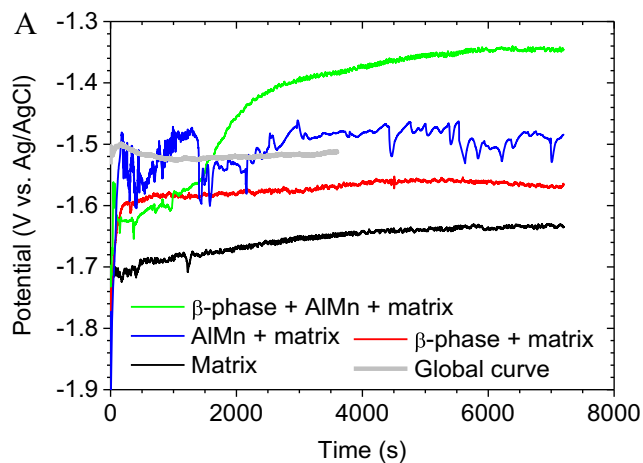

Fig. 2 **a** Evolution of the OCP of AZ91 in 0.1 M NaCl at the local (capillary diameter of 35 μm) and global scales. Experiments were performed after mechanical polishing. **b** Optical micrograph showing the different sites where local measurements were carried out (capillary positions indicated by *circles*)
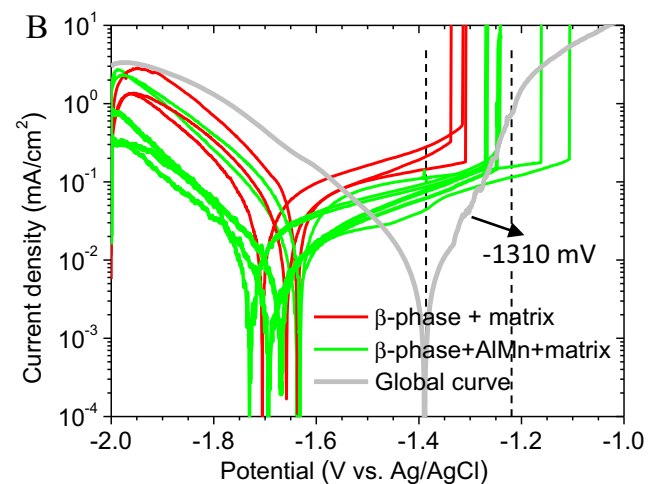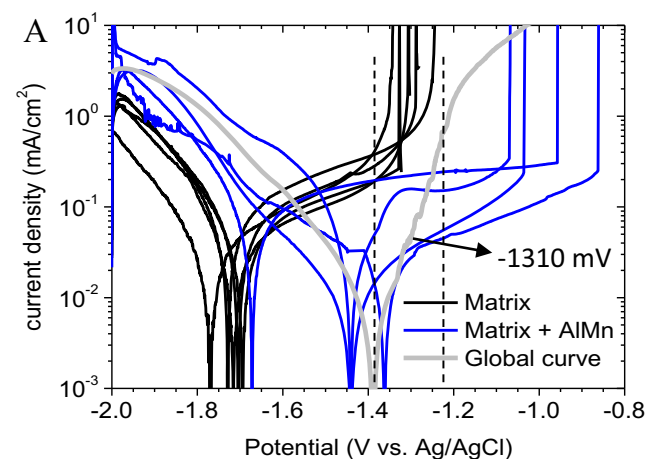

Fig. 3 **a–b** Polarisation curves (1 mV s^{-1}) in 0.1 M NaCl at the local (35 μm diameter capillaries) and global scales. Experiments were performed after mechanical polishing

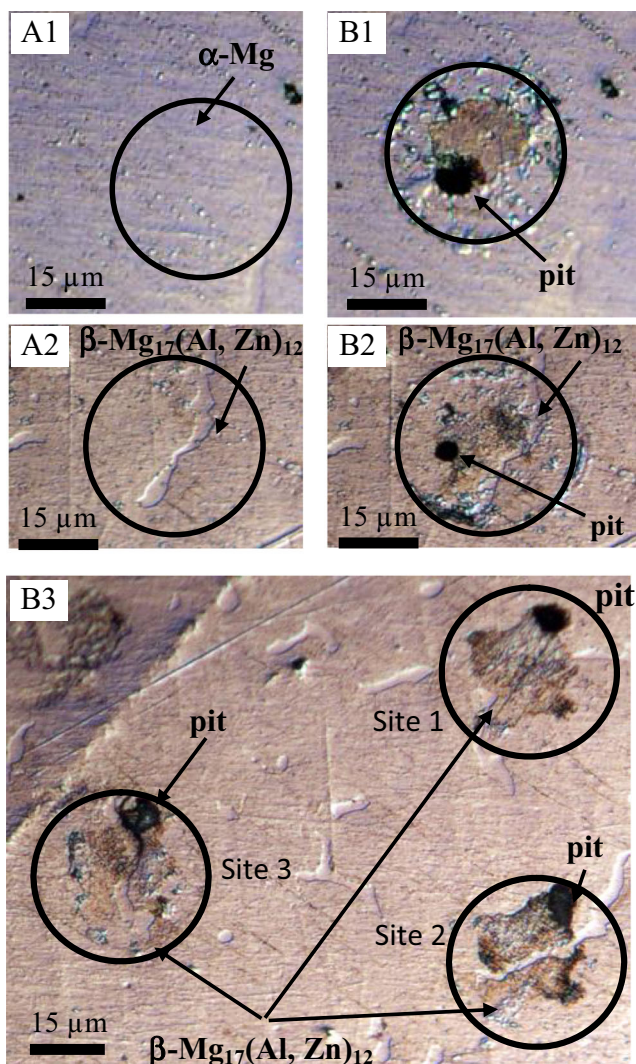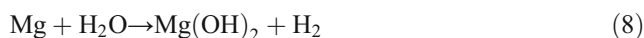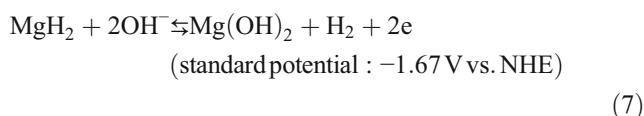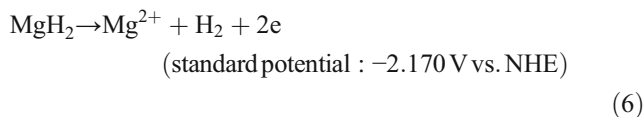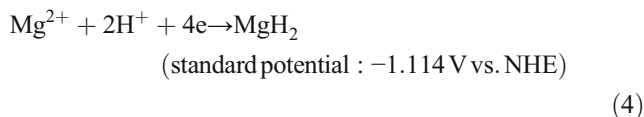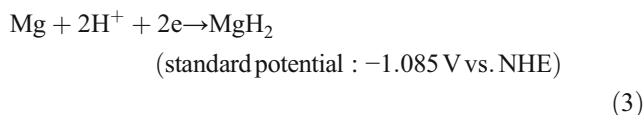**Fig. 4** Optical micrographs of the AZ91 surface after: (*a1–a2*) mechanical polishing and (*b1–b3*) local electrochemical measurements (polarisation curves) in 0.1 M NaCl. The diameter of the capillary (black circles) was 35 μm

by the presence of AlMn. Indeed, when comparing polarisation curves measured in the matrix with AlMn (blue curves in Fig. 3a) and the matrix with both β-phase and AlMn (green curves in Fig. 3b), the presence of β-phase clearly affects the current density in the cathodic branch and open circuit potential.

Other sites remain passive up to greater applied potentials. A large dispersion in pitting potentials is observed in the presence of AlMn precipitates (blue curves in Fig. 3a). Indeed, they range between −1300 and −850 mV vs. Ag/AgCl, indicating that these sites were generally more resistant to pitting corrosion than the matrix. This behaviour can be linked to the enrichment in Al observed in the matrix surrounding AlMn. These particles are mainly located at the α-Mg dendrites boundaries (region enriched in Al), Fig. 1. Moreover, recent work has confirmed the beneficial effect of Mn on corrosion resistance of AZ91 alloy [45].

To confirm previous results, a global chronoamperometry test was performed at −1310 mV vs. Ag/AgCl for 60 s. Figure 5a shows an optical micrograph of the specimen surface after this test. The metallic matrix underwent strong dissolution. Numerous pits are observed in the matrix, most of which are located in the centre of α-Mg dendrites where the aluminium content is low (less than 3 at.%, Table 1 and reference [37]). The average pit diameter is 20 μm, although a few of the pits are larger than this. By contrast, the β-Mg_{17}(Al, Zn)$_{12}$ and AlMn phases did not undergo dissolution. Therefore, previous assumptions are confirmed. Figure 5b shows the specimen surface after global chronoamperometry test at −1310 mV vs. Ag/agCl for 60 s. FE-SEM/EDS analysis was performed in different sites visible in Fig. 5b containing β-Mg_{17}(Al, Zn)$_{12}$ (site 1 in Fig. 5b), the matrix (sites 2 and 3 in Fig. 5b) and AlMn intermetallic particles (site 4 in Fig. 5b). Data are reported in Table 2. It can be seen that the surface is generally slightly oxidised (oxygen content around 2–3 at.%). Sites containing AlMn intermetallic particles are the most oxidised sites (oxygen content around 25 at.% in Table 2). No highly resistant oxide film covers the specimen surface. This explains why only pitting corrosion is observed (and not filiform corrosion).

Under these conditions, corrosion of magnesium and its alloys—which involves substrate dissolution, Mg-hydroxide formation and hydrogen evolution—proceeds according to Reactions (1–7). The overall reaction is given by Reaction (8).
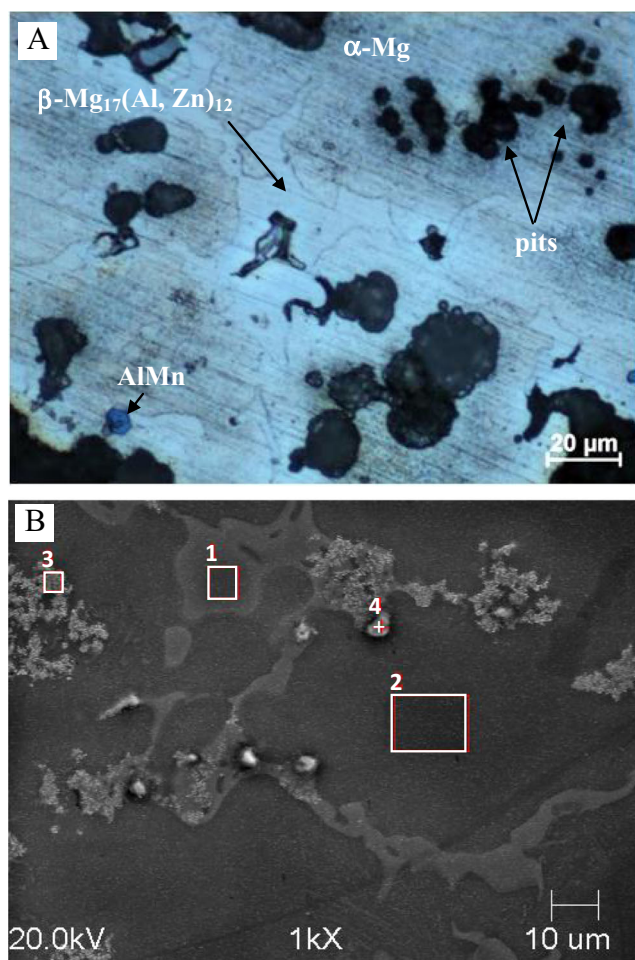
$$Mg \rightarrow Mg^{2+} + 2e$$
$$(\text{anodic reaction, standard potential} : -2.375\,V\,vs.\,NHE)$$
$$(1)$$

$$2H_2O + 2e \rightarrow H_2 + 2OH^-$$
$$(\text{cathodic reaction, standard potential} : -0.827\,V\,vs.\,NHE)$$
$$(2)$$

$$Mg + 2H^+ + 2e \rightarrow MgH_2$$
$$(\text{standard potential} : -1.085\,V\,vs.\,NHE)$$
$$(3)$$

$$Mg^{2+} + 2H^+ + 4e \rightarrow MgH_2$$
$$(\text{standard potential} : -1.114\,V\,vs.\,NHE)$$
$$(4)$$

$$Mg^{2+} + 2OH^- \rightarrow Mg(OH)_2 \qquad (5)$$

$$MgH_2 \rightarrow Mg^{2+} + H_2 + 2e$$
$$(\text{standard potential} : -2.170\,V\,vs.\,NHE)$$
$$(6)$$

$$MgH_2 + 2OH^- \leftrightarrows Mg(OH)_2 + H_2 + 2e$$
$$(\text{standard potential} : -1.67\,V\,vs.\,NHE)$$
$$(7)$$

$$Mg + H_2O \rightarrow Mg(OH)_2 + H_2 \qquad (8)$$

Fig. 5 **a** Optical and **b** SEM-FE micrographs of the AZ91 alloy surface after global chronoamperometry test in 0.1 M NaCl at −1310 mV vs. Ag/AgCl for 60 s

products may also contain Al-Mg-O compounds (maybe $MgAl_2(OH)_8*H_2O$). The presence of $MgAl_2(OH)_8*H_2O$ was already proposed in [46, 47]. Therefore, the main corrosion products should be $Mg(OH)_2$ and $MgAl_2(OH)_8*H_2O$. In addition, Baril and Pebere [48] found that the presence of oxygen did not influence the cathodic reaction during the corrosion of Mg.

In the case of AZ91 in 0.1 M NaCl, the cell geometry does not affect the electrochemical response of the system. The multiscale approach can then be used to investigate corrosion mechanisms. It was shown that (i) the matrix is prone to pitting corrosion, (ii) the β-phase has virtually no influence on the value of the pitting potential, and (iii) sites containing AlMn precipitates are more resistant to pitting corrosion, (iv) cathodic reactions preferentially occur at sites containing the matrix with AlMn. In addition, local measurements can be helpful to build a model with physical meaning (using relationships between electrochemical measurements and the microstructure described above) and to provide quantitative data (pitting potentials, cathodic current densities…) which can be used as boundary conditions in predictive numerical simulation. These quantitative data have never been quantified for AZ91 in the literature.

Global and local electrochemical behaviour of AZ91 in 0.1 M Na₂SO₄

The multiscale approach was also applied to AZ91 in 0.1 M Na_2SO_4. By contrast to 0.1 M NaCl, there is no good agreement between local and global measurements in 0.1 M Na_2SO_4. The OCP measured at the global scale increases continuously (to reach a value of about −1450 mV vs. Ag/AgCl after 7000 s of immersion), and no steady state is attained (grey curve in Fig. 6). This is attributed to the formation of a corrosion product film at the sample surface. As already discussed, the main corrosion products are $Mg(OH)_2$ and

The aluminium content in the matrix with corrosion products (Site 3, Table 2) is higher than that in the matrix (site 2, Table 2), indicating that the corrosion

Table 2 Chemical composition (in at.%) of various sites at the specimen surface (AZ91 alloy) determined by means of FE-SEM/EDS after different corrosion tests

|	Al	Mg	Zn	O	S	Cl	Mn
Site 1 in Fig. 5b, β-Mg₁₇(Al, Zn)₁₂	30.8	65.4	0.95	2.6	–	0.2	0
Site 2 in Fig. 5b, matrix	3.24	93	0	3.4	–	0.24	0
Site 3 in Fig. 5b, matrix with corrosion products	21.2	65.3	0.6	12.7	–	0.17	0
Site 4 in Fig. 5b, AlMn	36.8	12.4	0	25.3	–	0.1	23.7
Site 1 in Fig. 8a, β-Mg₁₇(Al, Zn)₁₂	32.1	60.2	1.9	5.5	0.28	–	0
Site 2 in Fig. 8a, matrix	5.7	64.7	0.5	28.5	0.6	–	0
Site 1, in Fig. 8b, matrix	7.7	23.8		64.6	4	–	0
Site 2 in Fig. 8b, β-Mg₁₇(Al, Zn)₁₂	32.1	59.9	2	5.9		–	0
Site 1 in Fig. 9c, β-Mg₁₇(Al, Zn)₁₂	28.3	64.9	1.8	4.8	0.4	–	0
Site 2 in Fig. 9c, matrix	4.4	63	0.2	30.9	1.6	–	0
Site 3 in Fig. 9c, eutectic	7.3	84.8	0.8	7	0.2	–	0
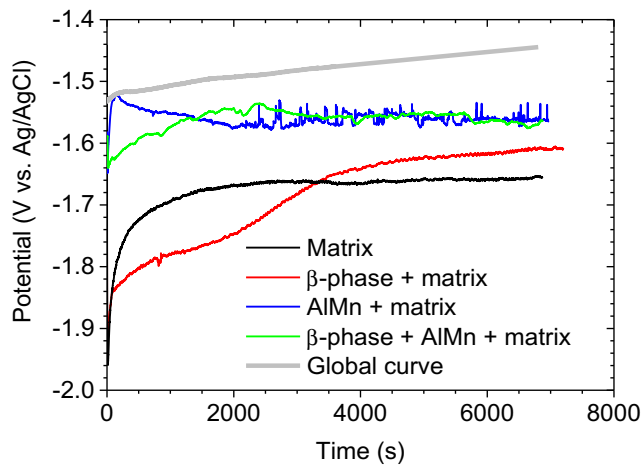
Fig. 6 Evolution of the OCP of AZ91 in 0.1 M Na$_2$SO$_4$ at the local (capillary diameter of 35 μm) and global scales. Experiments were performed after mechanical polishing

to reactions (1) and (9–10). Moreover, SO$_4^{2-}$ ions can be reduced, and reactions (11–12) can also proceed.

$$Mg^{2+} + 2Al^{3+} + 4SO_4^{2-} + 22H_2O \rightarrow MgAl_2(SO)_4 {*} 22H_2O \tag{9}$$

MgAl$_2$(OH)$_8$*H$_2$O. In aqueous solutions containing SO$_4^{2-}$ ions [47], corrosion of AZ91 alloy proceeds at OCP according
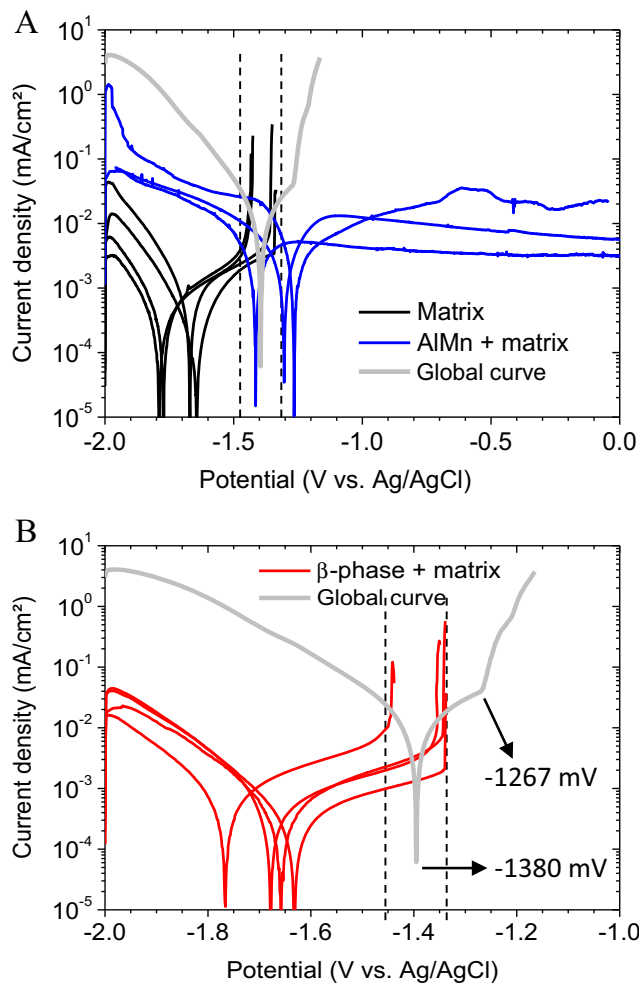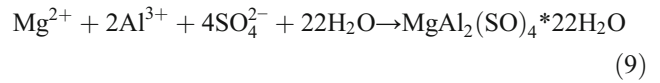
Fig. 7 **a–b** Local polarisation curves (35 μm diameter capillaries, 1 mV s^{-1}) for different sites in 0.1 M Na$_2$SO$_4$, after mechanical polishing. Global curves are also reported (grey curves)
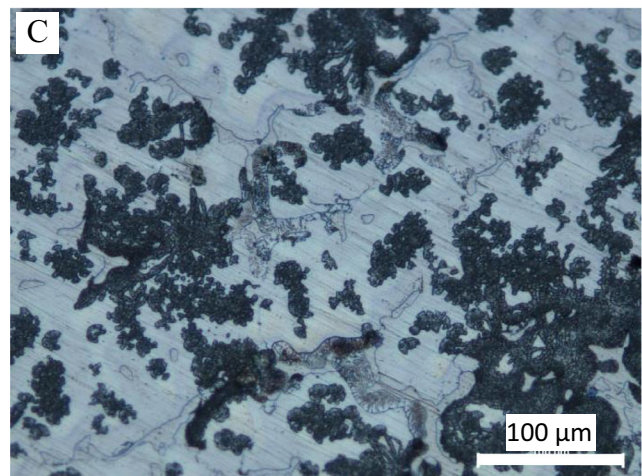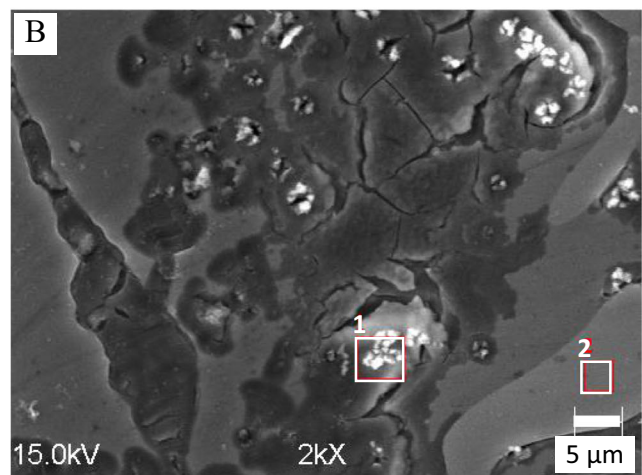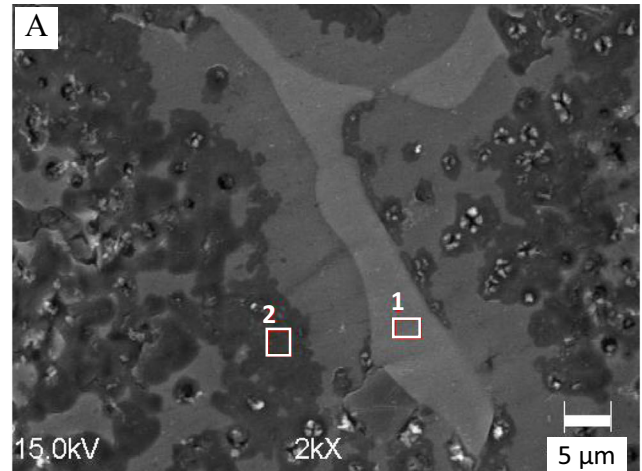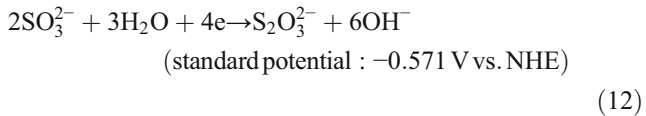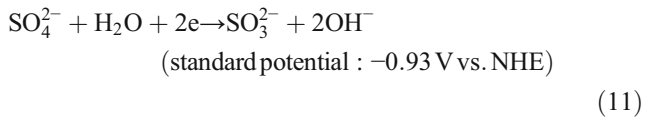

Fig. 8 **a–b** FE-SEM and **c** optical micrographs of the AZ91 surface after global chronoamperometry test in 0.1 M Na$_2$SO$_4$ at −1320 mV vs. Ag/AgCl for 60 s

$$Mg^{2+} + SO_4^{2-} \rightarrow MgSO_4 \qquad (10)$$

$$SO_4^{2-} + H_2O + 2e \rightarrow SO_3^{2-} + 2OH^-$$
$$(standard \, potential : -0.93 \, V \, vs. \, NHE) \qquad (11)$$

$$2SO_3^{2-} + 3H_2O + 4e \rightarrow S_2O_3^{2-} + 6OH^-$$
$$(standard \, potential : -0.571 \, V \, vs. \, NHE) \qquad (12)$$

Alkalization of the solution and formation of $Mg(OH)_2$ at the specimen surface are expected (reactions (2), (11) and (12)). This may hinder the formation of MgH_2 in 0.1 M Na_2SO_4 solution.

By contrast, a steady state is attained at the local scale for all investigated sites after approximately 4000 s of immersion (Fig. 6). The OCP values determined at the local scale (between −1660 and −1560 mV vs. Ag/AgCl) are shifted to the cathodic direction compared to that measured at the global scale (−1450 mV vs. Ag/AgCl). This suggests that no film was formed during the local tests. Therefore, one may assume that dissolved oxygen may be quickly consumed in the capillary near the specimen surface preventing both strong oxidation of the matrix and the formation of the corrosion products

film. By contrast, dissolved oxygen is not quickly consumed in the classical three-electrode cell near the specimen surface, and strong oxidation is observed. In the case of AZ91 in 0.1 M Na_2SO_4, the cell geometry seems to affect the corrosion mechanisms, and the electrochemical microcell technique has to be used carefully. The current density measured in the cathodic domain of local polarisation curves is significantly lower than that measured at the global scale (Fig. 7). Cathodic reactions correspond to dissolved oxygen and water reduction. Therefore, this confirms that dissolved oxygen may be quickly consumed in the capillary near the specimen surface and that under these conditions, the electrochemical microcell technique has to be used carefully. Additionally, the strong alkalization of the environment (reduction reactions: (2), (11) and (12)) has significant influence on the corrosion behaviour at the local scale.

The global polarisation curve of AZ91 obtained with the Na_2SO_4-based solution reveals the presence of a two-stage breakdown mechanism (grey curve in Fig. 7). The first stage occurs for applied potentials greater than $E_{b1} = -1380$ mV vs. Ag/AgCl. During this stage, the current density increases slowly. Global chronoamperometry measurements were performed within this region at −1320 mV vs. Ag/AgCl for 60 s, and the surface changes that were induced were quantified by
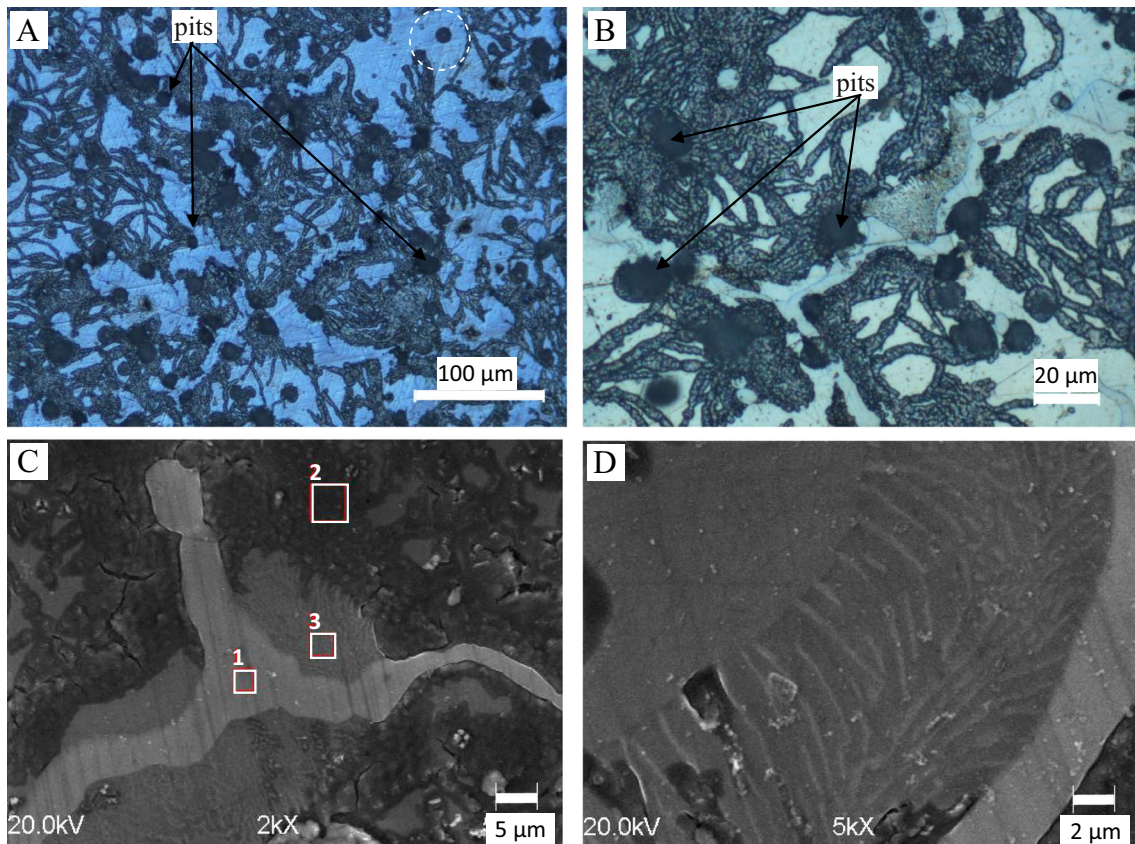

Fig. 9 **a–b** Optical and **c–d** FE-SEM micrographs of the AZ91 surface after global chronoamperometry test in 0.1 M Na_2SO_4 at −1240 mV vs. Ag/AgCl for 60 s

using optical miroscopy and FE-SEM/EDS (Fig. 8). The matrix is heavily oxidised. Indeed, a large amount of oxygen was detected by means of FE-SEM/EDS measurements in the matrix (site 2 of Fig. 8a and site 1 of Fig. 8b, results in Table 2). The fact that sulphur species were detected indicates that SO_4^{2-} ions are adsorbed. We also found that β-$Mg_{17}(Al, Zn)_{12}$ is slightly oxidised (site 1 of Fig. 8a and site 2 of Fig. 8b, results in Table 2). The slight oxidation at these last two sites (β-phase) is caused by the presence of a high amount of aluminium in the particles. In addition, small quantities (less than 0.3at.% in Table 2) of sulphur species were detected at these two sites. Therefore, the evolution of the current density observed in the first stage of the polarisation curve can be attributed to the formation of $Mg(OH)_2$, which hinders anodic reactions and the adsorption of SO_4^{2-} ions. Optical observations conducted at low spatial resolution indicate that oxidation occurs over the whole specimen surface (Fig. 8c). These observations also reveal that filiform corrosion starts during the first stage of the polarisation curves. This corrosion mode is observed because of the formation of a highly resistant oxide film due to strong oxidation of the surface during this stage.

The second stage of the polarisation curve corresponds to potentials greater than $E_{b2}=-1270$ mV vs. Ag/AgCl and is characterised by a rapid rise in the anodic current density. Global chronoamperometry measurements were performed at -1240 mV vs. Ag/AgCl for 60 s (second region of the polarisation curve, grey curve in Fig. 7). Optical microscopy conducted after this test reveals the presence of numerous pits with a diameter of approximately 20 μm at the specimen surface (Fig. 9a, b). The evolution of the current density in the second stage of the polarisation curve can be attributed to the breakdown of the $Mg(OH)_2$ film (formed during the first stage) and the dissolution of the alloy. A surface analysis revealed that sites located within the matrix (away from pits), eutectic structure and β-$Mg_{17}(Al, Zn)_{12}$ all have roughly the same chemical composition as in the first stage. Results derived from EDS measurements corresponding to the sites visible in Fig. 9c are reported in Table 2. These results also show that the sample is not significantly oxidised during the second stage of the polarisation curve. However, the α-Mg solid solution located between the ultrathin β-$Mg_{17}(Al, Zn)_{12}$ precipitates in the eutectic structure starts to oxidise (Fig. 9d). This is not observed in the first region of the polarisation curve (Fig. 7).

After the alloy was immersed in 0.1 M Na_2SO_4 at -1240 mV vs. Ag/AgCl (second stage) for 60 s, filiform corrosion continues to grow. This is clearly visible in Fig. 9a, b. We also observe that filaments propagate in different directions and never intersect. It appears that a filament would stop in its path upon encountering another filament. Observations conducted at high spatial resolution (Fig. 10a, b) reveal that no filaments propagate in either the eutectic structure or the β-phase. Indeed, they only propagate in the α-Mg matrix. The reason for the development of such filiform corrosion is that a resistant oxide film was
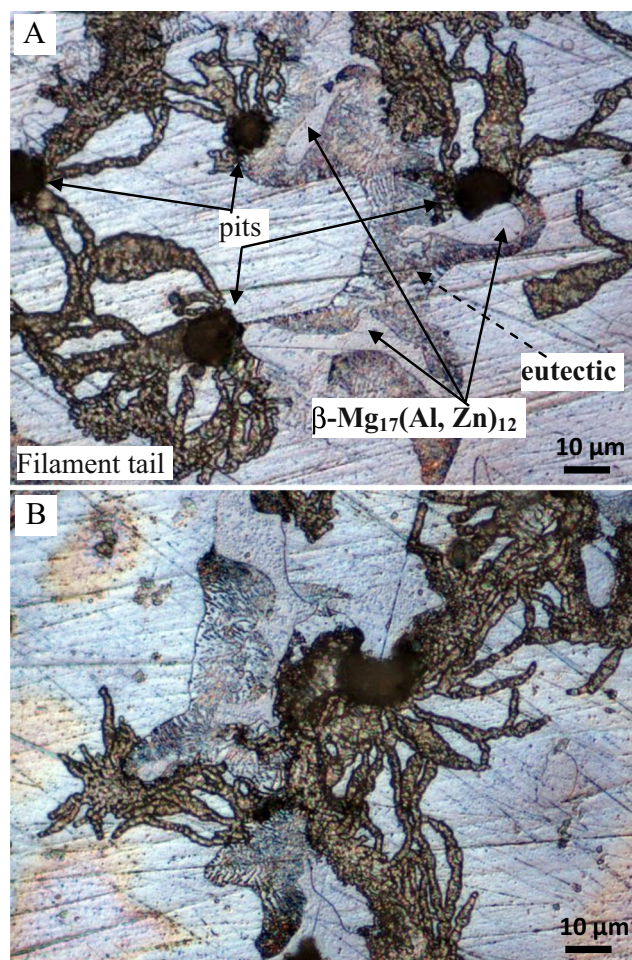
Fig. 10 a–b Optical micrographs of the AZ91 surface after global chronoamperometry test in 0.1 M Na_2SO_4 at -1240 mV vs. Ag/AgCl for 60 s

formed on the matrix during the first stage. The presence of this resistant surface film was revealed by EDS measurements. Filiform corrosion has previously been observed in pure magnesium [13, 49–56] as well as Mg–Al [57, 58], Mg–Y [50], Mg–8Li [55], AM30 [59], AZ31 [60, 61], AZ80 [60], AZ91D [13] and AZ91 [51] alloys after immersion in chloride-containing solutions. It has been found that the propagation of filaments occurs with voluminous gas evolution at the head while the body immediately behind it passivates [62]. Filiform corrosion has been observed in high purity magnesium of unpolarised and galvanostatically polarised specimen in aqueous sodium chloride electrolyte [52, 56]. A relatively widespread surface coverage of what is the typically observed filiform-like corrosion morphology [63] was observed for pure Mg. The presence of alloyed As (0.37 %) decreases cathodic reaction and modifies the resultant corrosion morphology upon Mg, mitigating the typically observed filiform-like corrosion [64]. It has also been established that the cathodic reaction of filiform corrosion in magnesium alloys is driven by hydrogen evolution [48]. To our knowledge, until now, filiform corrosion has never been observed in Mg alloys in Na_2SO_4-based solutions.

Numerous pits also initiate during the second stage (Figs. 9a, b and 10). The filiform corrosion appears to be the forerunner of regular pitting [16]. Indeed, only one pit, encircled in Fig. 9a, was not connected to any filaments.

According to local measurements, sites containing the matrix located in the centre of dendrites (black curve in Fig. 7a) and sites containing the matrix close to β-phase (red curve in Figs. 7a and 11(a1) and (b1)) undergo pitting corrosion during the first stage of the global polarisation curve. Sites containing the matrix+AlMn remain passive up to 0 mV vs. Ag/AgCl.
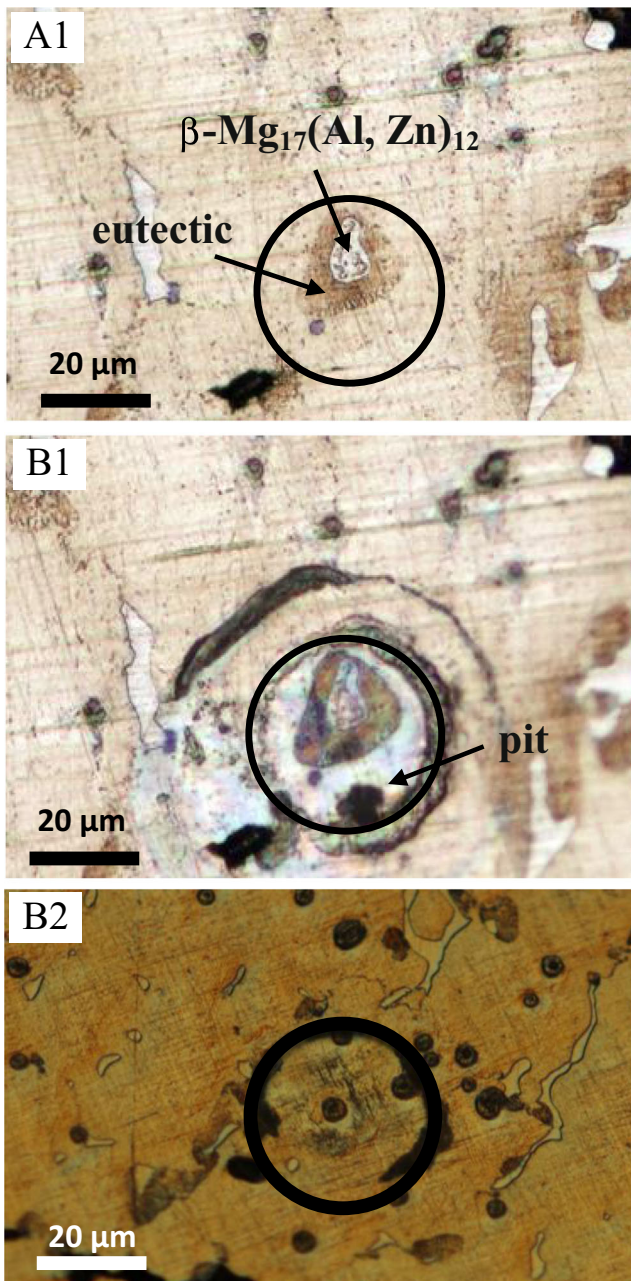

Fig. 11 Optical micrographs of the AZ91 surface after: (*a1*) mechanical polishing and (*b1–b2*) local electrochemical measurements (polarisation curves) in 0.1 M Na₂SO₄. The diameter of the capillary (black circles) was 35 μm

(blue curves in Fig. 7a). This is confirmed from surface observations (Fig. 11(b2)). Filiform corrosion is never observed using local techniques. As it was already demonstrated by means of OCP vs. time (Fig. 6) and local polarisation curves (Fig. 7), the amount of dissolved oxygen quickly decreases in the capillary, preventing the formation of a resistant oxide film. Under these specific conditions, filiform corrosion cannot develop. Indeed, this type of corrosion is typically associated with a metal surface having a protective coating or a highly resistant oxide film.

To confirm the previous hypothesis, global chronoamperometry test was performed at −1240 mV vs. Ag/AgCl for 60 s in deaerated 0.1 M Na₂SO₄. The solution was deaerated by bubbling with argon gas for 1 h. The content of dissolved oxygen in the solution is then low. These conditions are close to those found in the capillary (although it is impossible to measure the content of dissolved oxygen in the capillary). As shown in Fig. 12, filiform corrosion is significantly hindered. Only a few filaments are visible, whereas numerous filaments are observed after global chronoamperometry test in aerated 0.1 M Na₂SO₄ (Fig. 9a). This confirms the effect of the oxygen content on the corrosion behaviour to explain the occurrence of the filiform corrosion of AZ91 in 0.1 M Na₂SO₄ only in the global-scale measurement.

Conclusions

AZ91 has a complex microstructure. The microstructure and corrosion behaviour of as-cast AZ91 alloy was studied. The following conclusions can be drawn:

1. The results obtained in 0.1 M NaCl indicate that only pitting occurs in the alloy. Slight oxidation of the matrix is detected by means of FE-SEM/EDS. Both local and
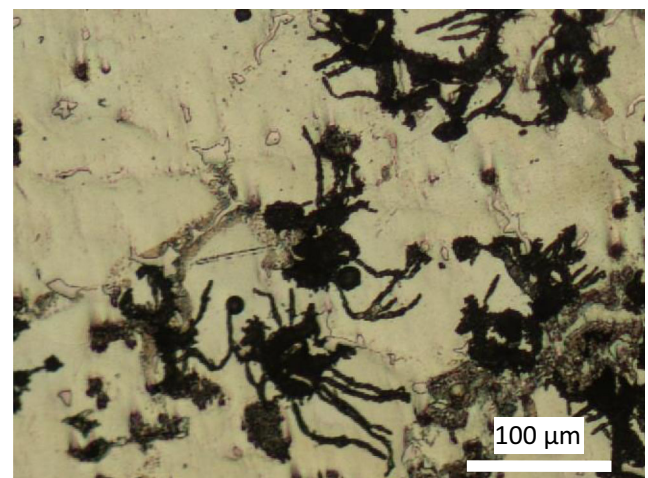

Fig. 12 Optical micrograph of the AZ91 surface after global chronoamperometry test in deaerated 0.1 M Na₂SO₄ at −1240 mV vs. Ag/AgCl for 60 s

global measurements show that AlMn precipitates have the highest corrosion resistance owing to Al enrichment at these sites, whereas the α-Mg (matrix) phase is the most susceptible to corrosion. Numerical values of pitting potentials and current densities in the cathodic branch and in the current plateau have been proposed. Under these conditions (only pitting corrosion is observed), the multiscale approach can be applied to AZ91 in 0.1 M NaCl.

2. By contrast, the multiscale cannot be applied to AZ91 in 0.1 M Na_2SO_4 because corrosion mechanisms were affected by the microcell geometry. Using the classical cell, a two-stage breakdown mechanism has been identified for corrosion in Na_2SO_4 solution. During the first stage, a highly resistant oxide film forms on the matrix, while AlMn precipitates and the β-phase undergo slight oxidation. Fifliform also starts to grow (due to the presence of the highly resistant oxide film at the specimen surface). During the second stage, pitting occurs in the matrix, and filiform corrosion continues to grow. Filiform corrosion is not observed using local techniques. It was proposed that the dissolved oxygen is quickly consumed in the capillary, preventing strong oxidation of the specimen surface (and therefore preventing filiform corrosion). This was confirmed from global chronoamperometry test performed in deaerated solution. Under these conditions, filiform corrosion is significantly hindered.

These results show that the local techniques have to be used carefully and that local measurements have to be validated before being used to understand corrosion mechanisms. Additional experiments will be performed to explain definitively why the different local conditions in the microcell as compared with the classical electrochemical cell lead to such drastic differences in the corrosion mode in Na_2SO_4 but not in NaCl.

References

1. Ghali E, Dietzel W, Kainer KU (2004) J Mater Eng Perform 13:517–529
2. Kojima Y (2000) Mater Sci Forum 350–351:3–17
3. Shaw BA (2003) Corrosion fundamentals, testing and protection. ASM Int ASM Handb 13A:692–696
4. Singh Raman RK (2004) Metall Mater Trans 35A:2525–2531
5. Zhang L, Cao ZY, Liu YB, Su GH, Cheng LR (2009) Mater Sci Eng 508A:129–133
6. Fan Y, Wu G, Zhai C (2066) Mater Sci Eng 433A:208–215
7. Srinivasan A, Ningshen S, Kamachi Mudali U, Pillai UTS, Pai BC (2007) Intermetallics 15:1511–1517
8. Sudholz AD, Birbilis N, Bettles CJ, Gibson MA (2009) J Alloys Compd 471:109–115
9. Wu G, Fan Y, Gao H, Zhai C, Zhu YP (2005) Mater Sci Eng 408A:255–263
10. Zhou W, Aung NN, Sun Y (2009) Corros Sci 51:403–408
11. Nam ND, Bian MZ, Forsyth M, Seter M, Tan M, Shin KS (2012) Corros Sci 64:263–271
12. Abidin NIZ, Martin D, Atrens A (2011) Corros Sci 53:862–872
13. Ambat R, Aung NN, Zhou W (2000) Corros Sci 42:1433–1455
14. Anik M, Avci P, Tanverdi A, Celikyurek I, Baksan B, Gurler R (2006) Mater Des 27:347–355
15. Bonora PL, Andrei M, Eliezer A, Gutman EM (2002) Corros Sci 44:729–749
16. Ghali E, Dietzel W, Kainer KU (2004) J Mater Eng Perform 13:7–23
17. Jonsson M, Thierry D, LeBozec N (2006) Corros Sci 48:1193–1208
18. Lunder O, Aune TKR, Nisancioglu K (1987) Corrosion 43:291–295
19. Lunder O, Lein JE, Aune TK, Nisancioglu K (1989) Corrosion 45:741–748
20. Lunder O, Nordlien JH, Nisancioglu K (1997) Corros Rev 15:439–469
21. Mathieu S, Rapin C, Hazan J, Steinmetz P (2002) Corros Sci 44:2737–2756
22. McIntyre NS, Chen C (1998) Corros Sci 40:1697–1709
23. Pardo A, Merino MC, Coy AE, Viejo F, Arrabal R, Feliu S Jr (2008) Electrochim Acta 53:7890–7902
24. Song GL, Atrens A (1999) Adv Eng Mater 1:11–33
25. Song GL, Atrens A (2003) Adv Eng Mater 5:837–858
26. Song G, Atrens A, Dargusch M (1999) Corros Sci 41:249–273
27. Song G, Atrens A, St. John D, Wu X, Nairn J (1997) Corros Sci 39:1981–2004
28. Song G, Atrens A, St. John D, Nairn J (1997) Corros Sci 39:855–875
29. Song G, Atrens A, Wu X, Zhang B (1998) Corros Sci 40:1769–1791
30. Song G, Bowles AL, St. John DH (2004) Mater Sci Eng 366A:74–86
31. Zhang T, Shao Y, Meng G, Cui Z, Wang F (2011) Corros Sci 53:1960–1968
32. Zhao MC, Liu M, Song G, Atrens A (2008) Corros Sci 50:1939–1953
33. Sudholz AD, Kirkland NT, Buchheit RG, Birbilis N (2001) Electrochem Solid State Lett 14:C5–C7
34. Yang LJ, Li YF, Wei YH, Hou LF, Li YG, Tian Y (2010) Corros Sci 52:2188–2196
35. Galicia G, Pebere N, Tribollet B, Vivier V (2009) Corros Sci 51:1789–1794
36. Chen J, Wang J, Han EH, Ke W (2009) Corros Sci 51:477–484
37. Krawiec H, Stanek S, Vignal V, Lelito J, Suchy JS (2011) Corros Sci 53:3108–3113
38. Singh Raman RK, Birbilis N, Efthimiadis J (2004) Corros Eng Sci Technol 39:346–350
39. Amar H, Vignal V, Krawiec H, Josse J, Peyre P, da Silva SN, Dick LF (2011) Corros Sci 53:3215–3221
40. Bohni H, Suter T, Assi F (2000) Surf Coat Technol 130:80–86
41. Jorcin JB, Krawiec H, Pébère N, Vignal V (2009) Electrochim Acta 54:5775–5781
42. Krawiec H, Vignal V, Akid R (2008) Electrochim Acta 53:5252–5259
43. Krawiec H, Vignal V, Heintz O, Ponthiaux P, Wenger F (2008) J Electrochem Soc 155:C127–C130
44. Suter T, Bohni H (2001) Electrochim Acta 47:191–199

45. Xiaoyan L, Mingzhao L, Liuqun F, Haiyan W, Chong F, Hua M (2014) Rare Metal Mater Eng 43:0278–0282

46. Chen J, Wang J, Han E, Dong J, Ke W (2006) Mater Corros 57: 789–793

47. Chen J, Wang J, Han E, Dong J, Ke W (2007) Electrochim Acta 52: 3299–3309

48. Baril G, Pebere N (2001) Corros Sci 43:471–484

49. Hiromoto S, Yamamoto A, Maruyama N, Somekawa H, Mukai T (2008) Corros Sci 50:3561–3568

50. Liu M, Schmutz P, Uggowitzer PJ, Song G, Atrens A (2010) Corros Sci 52:3687–3701

51. Lunder O, Lein JE, Hsjevik SM, Aune TKR (1994) Werkst Korros 45:331–340

52. Ralston KD, Williams G, Birbilis N (2012) Corrosion 68:507–517

53. Ruggeri RT, Beck TR (1983) Corrosion 39:452–465

54. Schmutz P, Guillaumin V, Lillard RS, Lillard JA, Frankel GS (2003) J Electrochem Soc 150:B99–B110

55. Song Y, Shan D, Chen R, Han EH (2009) Corros Sci 51:1087–1094

56. Williams G, Birbilis N, McMurray HN (2013) Electrochem Commun 36:1–5

57. Hara N, Kobayashi Y, Kagaya D, Akao N (2007) Corros Sci 49: 166–175

58. Nisancioglu K, Lunder O, Aune TKR (1990) In: Proc. 47th Annual World Magensium Conference, Cannes, France, 43–50

59. Song W, Martin HJ, Hicks A, Seely D, Walton CA, Lawrimore WB, Wang PT, Horstemeyer MF (2014) Corros Sci 78:353–368

60. Feliu S Jr, Pardo A, Merino MC, Coy AE, Viejo F, Arrabal R (2009) Appl Surf Sci 255:4102–4108

61. Wang L, Shinohara T, Zhang BP (2009) Mater Trans 50:2563–2569

62. Lunder O, Lein JE, Hesjevik SM, Aune TKr, Nisancioglu K (1990) In: Proc. 11th Annual Corrosion Congress, Florence (Italy) 5.255-5.262

63. Williams G, McMurray HN (2008) J Electrochem Soc 155:C340

64. Birbilis N, Williams G, Gusieva K, Samaniego A, Gibson MA, McMurray HN (2013) Electrochem Commun 34:295–298